metals

MDPI

Article

Exceptional Phase-Transformation Strengthening of $Fe_{50}Mn_{20}Cr_{20}Ni_{10}$ Medium-Entropy Alloys at Cryogenic Temperature

Zhong Wang [1], Mingjie Qin [2], Min Zhang [2], Huijun Yang [2,3], Junwei Qiao [2,3,*] and Zhihua Wang [1,*]

[1] Institute of Applied Mechanics, College of Mechanical and Vehicle Engineering, Taiyuan University of Technology, Taiyuan 030024, China; zhongwangty@hotmail.com
[2] College of Materials Science and Engineering, Taiyuan University of Technology, Taiyuan 030024, China; qinmingjie-0@hotmail.com (M.Q.); zm-821202@163.com (M.Z.); pineyang@126.com (H.Y.)
[3] Key Laboratory of Interface Science and Engineering in Advanced Materials, Ministry of Education, Taiyuan University of Technology, Taiyuan, 030024, China
* Correspondence: qiaojunwei@gmail.com (J.Q.); wangzh077@163.com (Z.W.)

Abstract: Cobalt-free $Fe_{50}Mn_{20}Cr_{20}Ni_{10}$ medium-entropy alloys were developed with the metastable engineering strategy at cryogenic temperature. The phase formation rules were calculated and the stacking fault energy was estimated at different temperatures. The uniaxial tensile tests were carried out at a cryogenic temperature and the mechanical properties were completely investigated, displaying excellent strain-hardening capacity. The deformation mechanisms were systematically explained by forest dislocation, twinning strengthening, and phase-transformation strengthening at cryogenic temperature. The precipitation of the second phase sacrifices some ductility, but still achieves excellent strong-plastic synergy.

Keywords: medium-entropy alloys; phase transformation; cryogenic temperature

Citation: Wang, Z.; Qin, M.; Zhang, M.; Yang, H.; Qiao, J.; Wang, Z. Exceptional Phase-Transformation Strengthening of $Fe_{50}Mn_{20}Cr_{20}Ni_{10}$ Medium-Entropy Alloys at Cryogenic Temperature. *Metals* **2022**, *12*, 643. https://doi.org/10.3390/met12040643

Academic Editor: Seok Su Sohn

Received: 18 February 2022
Accepted: 8 April 2022
Published: 10 April 2022

1. Introduction

With the rapid development of the aerospace, marine shipbuilding, and natural gas transportation industries, the demand for metallic alloys of ultra-high strength and exceptional ductility in cryogenic environments has increased. The dilemma in designing alloys is that many engineering structural materials become brittle at low temperatures, and their applications are generally limited at cryogenic temperatures [1–3]. Recently, a new class of materials, high-entropy alloys (HEAs), exhibiting excellent mechanical properties, has attracted much attention all around the world. The discovery of HEAs provides unprecedented opportunities for the material community to explore and obtain superb properties that are difficult to achieve in conventional alloys at cryogenic temperature, such as high strength and toughness [4,5].

The classic CoCrFeMnNi HEA, with the face-centered cubic (FCC) structure, shows excellent mechanical properties at cryogenic temperature, reaching the yielding strength of 1692 MPa and the uniform elongation of 10.3% at 77 K [4,6]. The properties are mainly attributed to the twinning-induced plasticity (TWIP) during deformation at cryogenic temperature. An FCC-structured $Fe_{60}Co_{15}Ni_{15}Cr_{10}$ shows strong strain-hardening ability at 77 K due to the deformation-induced phase transformation from FCC to body-centered cubic (BCC) phase [7]. With the decrease in temperature, the enhanced strain hardening capacity of $Fe_{40}Mn_{40}Co_{10}Cr_{10}$ HEA is attributed to the variation in deformation mechanisms from dislocation slip to twin formation and further to phase transformation [8]. It is obvious that phase transformation is an efficient method to improve the plasticity of the HEA at cryogenic temperature. However, the high cost of cobalt elements limits the prospect of engineering applications. Therefore, cobalt-free HEAs have been further designed and widely investigated. It is reported that a slight twinning strengthening can

obtain yielding strength, ultimate tensile strengths, and uniform elongation of 1.2 GPa, 1.34 GPa, and 22% at 77 K for $Fe_{40}Mn_{20}Cr_{20}Ni_{20}$ HEA, respectively [9]. At present, the emergence of metastability engineering has brought a new performance improvement direction, which has attracted much attention toward HEAs [10]. According to the metastability engineering strategy at cryogenic temperature, the aim of this study is to develop a new HEA for low-temperature potential application by optimizing the composition based on $Fe_{40}Mn_{20}Cr_{20}Ni_{20}$ HEA.

In order to achieve a metastable structure, decreasing the stacking fault energy (SFE) is a key factor. It is reported that reducing the Ni will lead to a low SFE [8]. By lowering SFE and the low-cost condition and introducing the transformation-induced plasticity (TRIP) effect, the $Fe_{50}Mn_{20}Cr_{20}Ni_{10}$ HEA was successfully designed by adjusting the composition ratio. Besides these factors, the entropy of mixing and some other criteria were calculated to further verify the phase formation. It is noted that the entropy of mixing of the current alloy is 1.22*R* (*R* is gas constant), which is within the scope of "medium entropy" according to the concept of "high-entropy alloys" [11]. Therefore, due to the contributions of both TRIP and TWIP effects, the newly developed $Fe_{50}Mn_{20}Cr_{20}Ni_{10}$ medium-entropy alloy (MEA) exhibits an excellent combination of strength and ductility at liquid-nitrogen temperature and will be further discussed in this study.

2. Materials and Methods

The nominal chemical composition of the MEA is $Fe_{50}Mn_{20}Cr_{20}Ni_{10}$ (atomic percent, at.%). Firstly, the raw materials of Fe, Cr, and Ni were melted in a Ti-gettered, high-purity argon atmosphere with high-purity elements (weight purity $\geq$ 99.9%) in a vacuum arc melting furnace three times. An additional 5 wt.% was added to compensate for the loss of the Mn element by evaporation during melting together with the ingots (preparation from arc melting furnace) in a vacuum induction melting furnace. Raw material and ingots were alloyed in a boron nitride (BN) crucible to make a master alloy ($Fe_{50}Mn_{20}Cr_{20}Ni_{10}$) of 400 g in weight three times to ensure the chemical homogeneity. The master alloy was molten and was poured into a rectangular copper mold (length: 30 mm, width: 30 mm, and height: 100 mm). The ingots were homogenized at 1200 °C for 6 h and then water quenched. After that, the thin plates were cut from the ingots with the dimension of ~100 mm length, ~30 mm width, and ~3.3 mm thickness by wire electrical discharge machining. The plates were cold rolled along the tensile direction from ~3.3 mm to 1 mm thickness with a step size of 0.1 mm each time. The plates with 70% pre-deformation were annealed at 1073 K, 1173 K, and 1273 K for 1 h, and subsequently water quenched.

The phase structure was characterized by X-ray diffraction (XRD) with a Rigaku UltimalV diffractometer (Rigaku Corporation, Osaka, Japan). The microstructure was examined by scanning electron microscope (SEM) at 15 kV with a Phenom XL (Phenom-World BV, Eindhoven, The Netherlands). Rectangular dog bone-shaped tensile specimens with a thickness of 1 mm were sectioned from the alloys by electrical discharge machining (EDM, Huadong CNC Machine Tool Co., Ltd., Taizhou, China). The gage length and width of the tensile specimens were 10 and 3 mm, respectively. Uniaxial tensile tests were carried out at room temperature and cryogenic temperature (77 K) by an Instron 5969 materials testing machine (Instron, a Division of Illinois Tool Works Inc. ITW, Norwood, MA, USA) at an initial strain rate of 1×10^{-3} s^{-1}. After tensile tests, the microstructure was performed by transmission electron microscopy (TEM) with a JEM-F200 microscope (JEOL, Tokyo, Japan) operating at 200 kV.

3. Results and Discussion

In order to verify the phase formation of the current MEA, several criteria were proposed, including the entropy of mixing (ΔS_{mix}), the enthalpy of mixing (ΔH_{mix}), the atomic-size mismatch (δ), and valence electron concentration (VEC). The entropy of mixing of a multi-component alloy can be expressed as [12]:

$$\Delta S_{\text{mix}} = -R\sum_{i=1}^{N} c_i \ln c_i \quad (1)$$

where R is the gas constant, N is the number of elements, and c_i is the atomic percentage of the i-th component. Based on Equation (1), it is clear that the entropy of mixing will reach the maximum value when the alloy is of equi-atomic ratio. The maximum entropy of mixing for four elements is 1.39R. For the current alloy, the entropy of mixing is 1.22R, which is manifested as a typical MEA.

The enthalpy of mixing (ΔH_{mix}) in the solid solution is followed as [12,13]:

$$\Delta H_{\text{mix}} = \sum_{i=1, i\neq j}^{N} \Omega_{ij} c_i c_j \quad (2)$$

where N is the number of elements, $\Omega_{ij} (= 4\Delta H_{AB}^{\text{mix}})$ is the regular solution interaction parameter between i-th and j-th elements, $\Delta H_{AB}^{\text{mix}}$ is the enthalpy of mixing in binary liquid alloys, c_i and c_j are the atomic percentages of the i-th and j-th elements. For the present MEA, the enthalpy of mixing is -1.68 kJ/mol. The negative mixing enthalpy means one or more compounds will stably form in the binary alloys [13]. With the increase in the number of elements, the enthalpy will rapidly increase and the number of single-phase solid solutions will continue to decrease [14]. In addition, it is easier to form the intermetallic compounds with an extremely negative enthalpy of mixing [15]. Therefore, larger negative enthalpy of formation leads to the formation of intermetallic compounds, while positive enthalpy of formation tends to lead to phase separation into end phases with lower mutual solubility. Only slightly positive or slightly negative enthalpy of mixing is beneficial to the formation of a solid solution. Here, this MEA is easy to form a solid solution in the solid phase as the mixing enthalpy is close to zero.

The atomic-size difference is to estimate the comprehensive effect in multi-component alloys, which is described as [12]:

$$\delta = \sqrt{\sum_{i=1}^{N} c_i (1 - r_i/\bar{r})^2} \quad (3)$$

where c_i is the atomic fraction of the i-th component, r_i is the atomic radius of the i-th constituent element, and $\bar{r} (= \sum_{i=1}^{n} c_i r_i)$ is the average atomic radius of the alloy. Zhang et al. found that the range of atomic-size mismatch should be less than 6.5% and the mixing enthalpy should range from -15 to 5 kJ/mol, which is favorable to the formation of single-phase solid solution [12]. The atomic-size mismatch of this alloy is 3.37, which shows that it is easy to form a solid solution [12,16].

The VEC plays a significant role in predicting the phase formation, which is defined as [17]:

$$\text{VEC} = \sum_{i=1}^{N} c_i (\text{VEC})_i \quad (4)$$

where $(\text{VEC})_i$ is the VEC of the i-th element. According to Equation (4), the VEC of the current MEA is calculated as 7.6. Generally, the VEC is used to estimate the phase stability of FCC and BCC in HEAs. If the VEC is between 6.87 and 8, both FCC and BCC phases will co-exist [17]. It is noted that the amount of BCC phase is minor at the boundary of 8 [17]. In this study, the alloys were homogenized before the mechanical tests, which is discussed in detail below.

Figure 1 exhibits the XRD pattern of the alloy, and the upper right corner is the amplification of the local area (2θ = 45°~65°) in the figure. In this way, it is obvious that the homogenization sample is a single FCC structure, and there are new precipitated phases, marked by the black arrow, in the annealing samples after cold rolling. After phase retrieval and corresponding SEM image analysis, the new precipitated particles should be intermetallic compound σ phase. When the Cr content is higher than 15 wt.%, it is

reasonable [18]. The same phenomenon was also found in FeMnCrNi alloy with an equal atomic ratio [19].

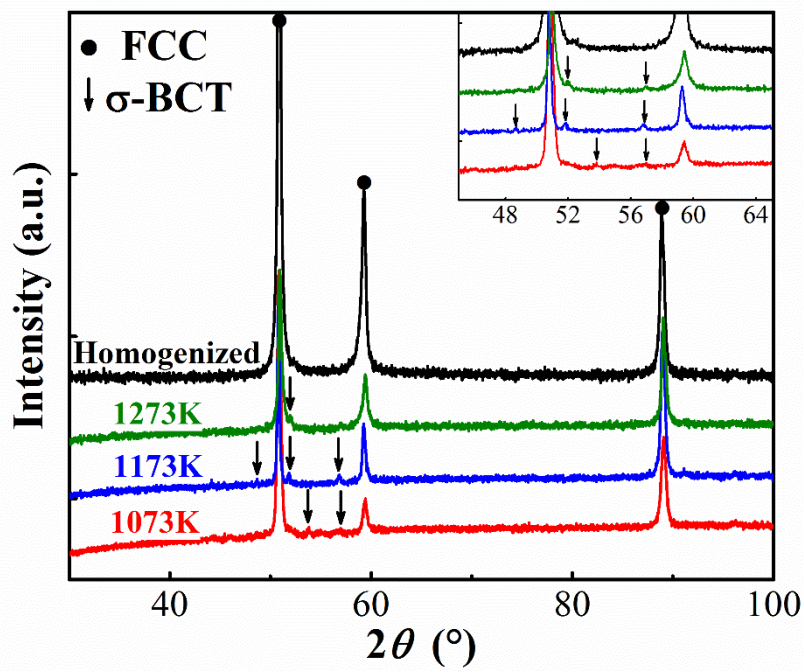

Figure 1. The XRD patterns of $Fe_{50}Mn_{20}Cr_{20}Ni_{10}$ MEA with different annealing states (including the homogenized sample).

Figure 2a presents an SEM image of the homogenized $Fe_{50}Mn_{20}Cr_{20}Ni_{10}$ MEA, which was composed of fully recrystallized equiaxed grains with an average grain size of ~100 μm. Further, it can be concluded that the crystal orientations were random without any texture. Figure 2b–d shows the microstructure after cold rolling and annealing. For the annealed microstructure at 1073 K, it can be clearly found that there are a small number of precipitates on the matrix, and complete recrystallization does not occur for the matrix. The distribution of precipitates is less in un-recrystallization regions. The alloy presents a complex microstructure of dual-phase and partial recrystallization. After annealing at 1173 K, it can be seen that the alloy has been fully recrystallized. The microstructure of the alloy annealed at 1273 K for 1 h has no obvious change compared with 1173 K, and the grain size and the size of the precipitated phase increase slightly. The σ particles are still insoluble at 1273 K.

Figure 3a shows a TEM image of the alloy annealed at 1273 K for 1 h after cold rolling at 70%. It can be found that spherical particles with a diameter of about 300 nm are precipitated on the matrix, and then selected area electron diffraction (SAED) is carried out for the (b) and (c) parts of the white virtual frame in the figure. The diffraction spots are shown in Figure 3b,c, respectively. It can be judged that the precipitated phase is the σ intermetallic compound and the matrix has an FCC structure, providing further evidence of XRD results.

Figure 4 shows the characteristic tensile engineering stress–strain curves of the $Fe_{50}Mn_{20}Cr_{20}Ni_{10}$ MEA at room temperature and cryogenic temperature. The yield strength ($\sigma_{0.2}$) ranges from 300 to 855 MPa under different heat treatments at room temperature. Meanwhile, the ultimate tensile strength (σ_u) is in the scope of 510 to 1005 MPa at room temperature. With the increase in heat treatment temperature from 1073 to 1273 K, the yield strength decreases while the uniform elongation (E_U) presents an increasing trend. At 77 K, the homogenization alloy shows a superior combination of yield strength of 605 MPa, ductility, defined as uniform elongation, of 42%, and ultimate tensile strength of 910 MPa, which were obviously better than those at 298 K. The mechanical properties of different annealed samples were also improved. The $\sigma_{0.2}$ reached 800 MPa, 975 MPa, and 1100 MPa, the σ_u reached 1235 MPa, 1320 MPa, and 1330 MPa, and the E_U was 38%, 19%, and 8%,

at 1273 K, 1173 K, and 1073 K, respectively. The tensile properties of the current alloy at cryogenic temperature are significantly better than those at room temperature. This phenomenon is very common in single-phase FCC HEAs [20]. The main cause is that dislocation slip is difficult at cryogenic temperature, which may stimulate a large number of deformation twins. However, the existence of precipitates still leads to the sacrifice of ductility. Overall, the cryogenic temperature mechanical performances of the FCC MEAs are of research significance.

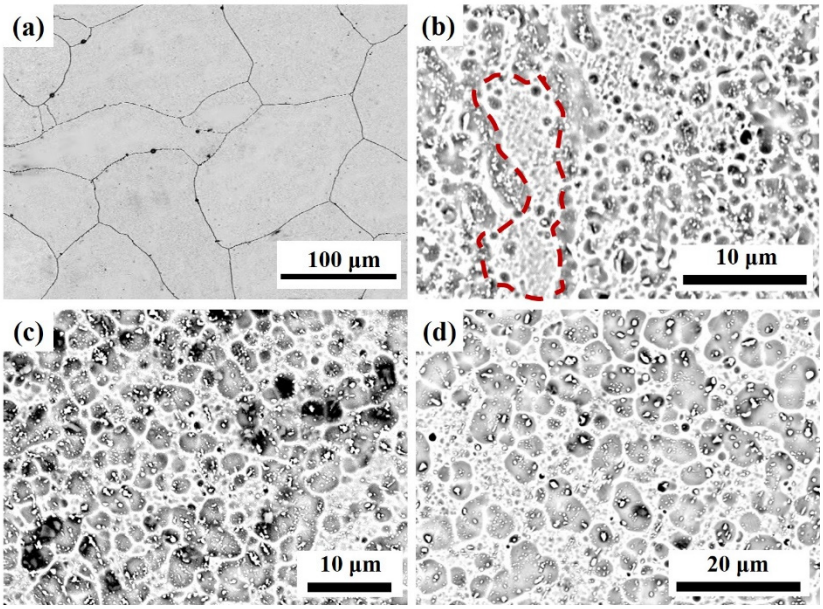

Figure 2. The SEM images of $Fe_{50}Mn_{20}Cr_{20}Ni_{10}$ at different states: (**a**) homogenized, (**b**) annealed at 1073 K for 1 h, (**c**) annealed at 1173 K for 1 h, (**d**) annealed at 1273 K for 1 h.

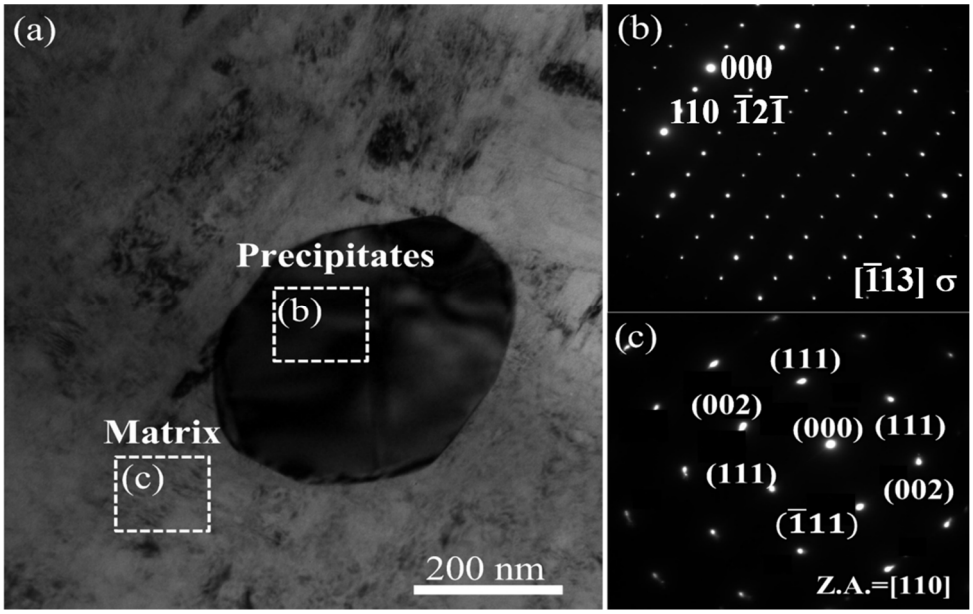

Figure 3. The bright-field TEM image of annealed $Fe_{50}Mn_{20}Cr_{20}Ni_{10}$ MEA at 1273 K for 1 h. (**b**,**c**) SAED patterns of the precipitate and matrix (marked by white dotted box) in (**a**), respectively.

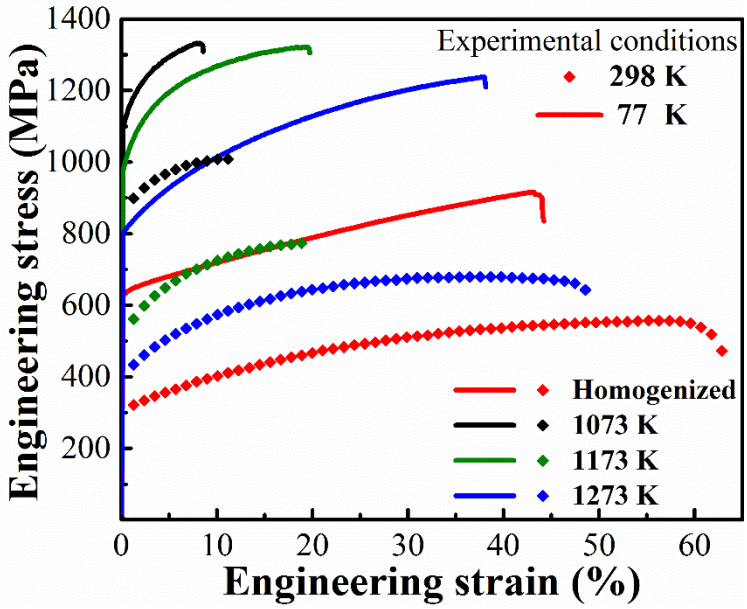

Figure 4. The cryogenic temperature tensile engineering stress–strain curves with different heat treatment conditions at 77 K.

Dislocation slip, twinning, and phase transformation are the three main deformation modes in FCC alloys. The ε-martensite transformation is controlled by the magnitude of the SFE [21]. The widely studied equi-atomic FeCoCrMnNi HEA has an SFE of ~25 mJ/m^2 at room temperature [22,23]. Reducing the contents of Ni and Co would lower the SFE of the current alloy and alloying costs, respectively, which promotes the potential industrial applicability of the alloys. According to the thermodynamic analysis, the ideal SFE of FCC phases in the present $Fe_{50}Mn_{20}Cr_{20}Ni_{10}$ MEA is then expressed by the following equation [24]:

$$Y_{SF} = 2\rho_A \Delta G^{\gamma \to \varepsilon} + 2\sigma^{\gamma \to \varepsilon} \quad (5)$$

where ρ_A is the molar surface density along planes, $\Delta G^{\gamma \to \varepsilon}$ is the molar Gibbs energy of the austenite to ε-martensite phase transformation, and $\sigma^{\gamma \to \varepsilon}$ is the interfacial energy per unit area of the phase boundary. The molar surface density ρ_A is calculated by Equation (6) [25]:

$$\rho_A = \frac{1}{16.8V^{\frac{2}{3}}} = \frac{4}{\sqrt{3}} \frac{1}{a^2 N} \quad (6)$$

where a = 0.365 nm is the lattice parameter of the alloy by XRD refinement, and N is Avogadro's number. Considering a regular solution model, $\Delta G^{\gamma \to \varepsilon}$ can be defined for the $Fe_{50}Mn_{20}Cr_{20}Ni_{10}$ MEA as:

$$\Delta G^{\gamma \to \varepsilon} = \sum_i X_i \Delta G_i^{\gamma \to \varepsilon} + \sum_j X_{Fe} X_j \Delta \Omega_{Fe}^{\gamma \to \varepsilon}{}_j \ (i = Fe,\ Mn,\ Cr,\ Ni;\ j = Cr,\ Mn,\ Ni) \quad (7)$$

where X_i and $\Delta G_i^{\gamma \to \varepsilon}$ represent the molar fraction and the difference in free energy between the FCC and hexagonal closed-packed (HCP) of pure metals. $\Delta \Omega_{Fe}^{\gamma \to \varepsilon}{}_j$ is an interaction energy parameter for components Fe and Mn, Cr, and Ni as the content of Fe in the FCC phase of the alloy is highest.

Substituting the obtained data listed in Table 1 into Equations (5)–(7), the relationship between the SFEs of the alloy and temperature is finally determined as:

$$Y_{SF} = 2.02 + 0.11T \ (\mathrm{mJ \cdot m^{-2}}) \quad (8)$$

Table 1. Numerical values and functions used for the calculations.

Parameter	Functions Used (Units)	Reference
$\Delta G_{\mathrm{Fe}}^{\gamma\to\varepsilon}$	$-2243.38 + 4.309T$ (J·mol^{-1})	[26]
$\Delta G_{\mathrm{Mn}}^{\gamma\to\varepsilon}$	$3970–1.7T$ (J·mol^{-1})	[27]
$\Delta G_{\mathrm{Cr}}^{\gamma\to\varepsilon}$	$1370–0.163T$ (J·mol^{-1})	[28]
$\Delta G_{Ni}^{\gamma\to\varepsilon}\Delta G_{\mathrm{Ni}}^{\gamma\to\varepsilon}$	$1046 + 1.255T$ (J·mol^{-1})	[26]
$\Delta\Omega_{\mathrm{FeMn}}^{\gamma\to\varepsilon}$	$-9135.5 + 15{,}282.1X_{\mathrm{Mn}}$ (J·mol^{-1})	[29]
$\Delta\Omega_{\mathrm{FeCr}}^{\gamma\to\varepsilon}$	2095 (J·mol^{-1})	[30]
$\Delta\Omega_{\mathrm{FeNi}}^{\gamma\to\varepsilon}$	2095 (J·mol^{-1})	[31]
a	3.65 Å	This work
$\sigma^{\gamma\to\varepsilon}$	0.008 (J·m^{-1})	[26]

Furthermore, 77 K and 298 K are substituted into Equation (8), and the SFEs of the alloys at both temperatures are acquired as:

$$\gamma_{\mathrm{SF}} = 34.8\ \mathrm{mJ{\cdot}m^{-2}} \quad 298\ \mathrm{K} \tag{9}$$

$$\gamma_{\mathrm{SF}} = 10.49\ \mathrm{mJ{\cdot}m^{-2}} \quad 77\ \mathrm{K} \tag{10}$$

To demonstrate the formation of HCP ε-martensite during plastic deformation, TEM micrographs of the region close to the fracture surface of the $Fe_{50}Mn_{20}Cr_{20}Ni_{10}$ alloy after the 77 K tensile test are presented in Figure 5.

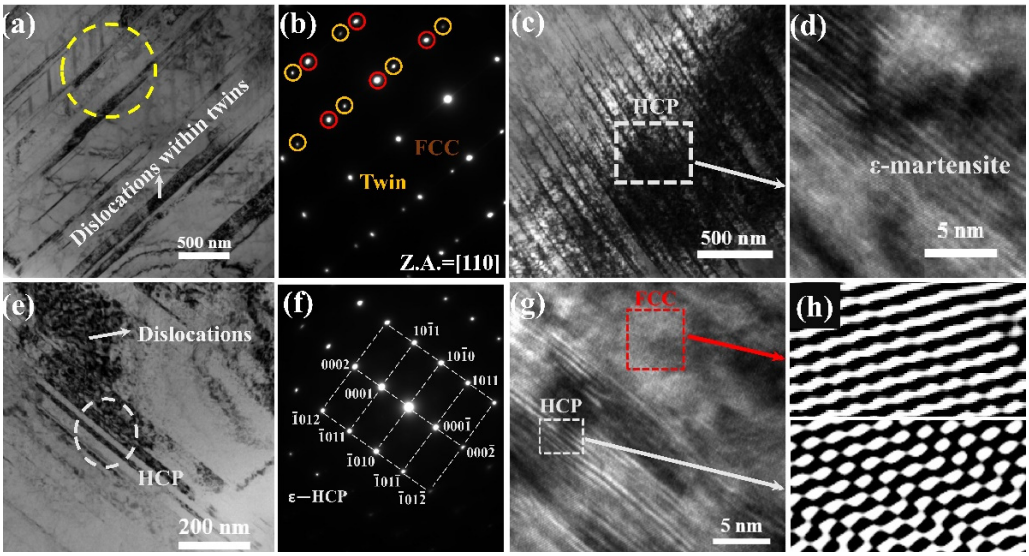

Figure 5. TEM micrographs of the region close to the fracture surface of the $Fe_{50}Mn_{20}Cr_{20}Ni_{10}$ alloy after 77 K tensile test showing (**a**) deformation twins and dense dislocations blocked by deformation twins, (**b**) diffraction pattern taken from the selected area (in yellow circle) of (**a**). (**c**) Image of the ε-martensite and (**d**) the corresponding HRTEM image. (**e**) Bright-field images of high-density dislocations around ε-martensite. (**f**) The diffraction pattern for the selected area (in red circle) of (**e**,**g**) the HRTEM observation. (**h**) Corresponding inverse fast Fourier transition (IFFT) images of the rectangle region in (**g**).

Figure 5a indicates the interaction between dislocations and deformation twins in the cryogenically deformed $Fe_{50}Mn_{20}Cr_{20}Ni_{10}$ alloy. The triggered deformation twins at cryogenic temperature contain high-density dislocations that act as strong barriers to dislocation glides, which further contributes to strain hardening. In addition, the abundant mechanical twinning in the $Fe_{50}Mn_{20}Cr_{20}Ni_{10}$ MEA also leads to a dynamic Hall-Petch effect (Figure 5a) [32,33]. The TWIP effect is also advantageous for the $Fe_{50}Mn_{20}Cr_{20}Ni_{10}$

alloy to have a higher ductility at 77 K [32]. The diffraction pattern of twins for the selected area (in Figure 5a, red circle) is shown in Figure 5b.

According to the HCP martensite nucleation model proposed by Mahajan et al. and the deformation twin formation model, the activation process of twins and martensites during deformation is discussed [34]. Firstly, the formation process of the HCP phase is the slip of Shockley partial dislocation on the spacer (111) crystal plane. The critical stress of HCP nucleus growth is displayed in Equation (11):

$$\tau_{tr} = \frac{2\sigma^{\gamma\to\varepsilon}}{3b_{tr}} + \frac{3Gb_{tr}}{L_{tr}} + \frac{h\Delta G^{\gamma\to\varepsilon}}{3b_{tr}} \quad (11)$$

where G is the shear modulus of the alloy, b_{tr} is the Burgers vector of the partial dislocation (0.147 nm), L_{tr} is the width of the HCP martensite nucleation, and h is the height of the martensite nucleation.

In FCC alloys, Mahajan and Chin [35] believed that the formation of deformed twins was the slip of a/6<112> Shockley partial dislocation on the continuous (111) crystal plane, and the critical size was used to describe the nucleation process of twins. The critical twin stress can be calculated by Equation (12):

$$\tau_{tw} = \frac{\gamma_{SF}}{3b_{tw}} + \frac{3Gb_{tw}}{L_{tw}} \quad (12)$$

where L_{tw} is the width of the twin nucleus (260 nm), and b_{tw} is the Burgers vector of a/6<112> Shockley partial dislocation. This study refers to the crystal plasticity model of high manganese steels [36], that is, the value of L_{tw}/L_{tr} is close to 1.5. Finally, the calculation results are multiplied by Taylor factor α (3.06), and the critical normal growth stresses of HCP martensites and twins are 742 MPa and 432 MPa, respectively. Combined with the stress–strain curve of the current alloy, it can be deduced that the TWIP process will continue once the plastic deformation begins. The TRIP mechanism will be activated after about 10% strain. This is close to the experimental results. The combined effect of these two mechanisms makes the work-hardening effect of the alloy very obvious, thus showing extremely excellent mechanical properties.

Figure 5c–h display dense dislocations that are accumulated around lath ε-martensites and the corresponding inverse fast Fourier transition (IFFT) images of the high-resolution TEM (HRTEM) FCC/HCP phase image. The transformation induced strain hardening, in addition to mechanical twinning and dislocation slip, and then contributes to the improvement in the strength and ductility. It is clear that the enhanced strength at cryogenic temperature originates not only from the increase in the dislocation density but more significantly from the continuously increasing number density and volume fraction of ε-martensites and twin boundaries. Therefore, the current alloy deformed at 77 K shows an exceptional strain-hardening capacity and strength–ductility combination. On the other hand, the precipitates form and rapid phase transformation occurs during the plastic deformation, which gives rise to the decrease in ductility of the present alloy.

4. Conclusions

In this study, a cobalt-free $Fe_{50}Mn_{20}Cr_{20}Ni_{10}$ MEA was developed by the metastable engineering strategy under low-temperature conditions. The microstructure was characterized by different methods and the mechanical deformation behavior was systematically studied at cryogenic temperature. The single-phase FCC MEA was obtained after homogenization treatment. After cold rolling and annealing treatment, Cr-rich intermetallic compound σ phase was precipitated from the FCC matrix, and the FCC + σ dual-phase structure was formed. At 77 K, the homogenization alloy showed a superior combination of yield strength of 605 MPa, uniform elongation of 42%, and ultimate tensile strength of 910 MPa. For different annealed samples, the yield strength reached 800 MPa, 975 MPa, and 1100 MPa, the ultimate tensile strength reached 1235 MPa, 1320 MPa, and 1330 MPa, and

the uniform elongation was 38%, 19%, and 8%, at 1273 K, 1173 K, and 1073 K, respectively. The strength of the alloy was significantly improved at cryogenic temperatures.

The combination of multiple deformation strengthening mechanisms of the homogenized alloy under cryogenic temperature, including forest-dislocation strengthening, twinning strengthening, and phase-transformation strengthening, leads to superb strain hardening capacity. Although the ductility decreases a little due to the existence of precipitates, the excellent cryogenic-temperature mechanical properties together with strength–ductility synergy are finally obtained.

Author Contributions: Z.W. (Zhong Wang) and M.Q. contributed equally to this work. Writing, Z.W. (Zhong Wang) and M.Q.; materials design, Z.W. (Zhong Wang), M.Q. and J.Q.; mechanical tests, M.Z.; data analysis, Z.W. (Zhong Wang), M.Q. and H.Y.; review and editing, J.Q. and Z.W. (Zhihua Wang); supervision, J.Q. and Z.W. (Zhihua Wang). All authors have read and agreed to the published version of the manuscript.

Funding: The authors would like to acknowledge the financial support of the Natural Science Foundation of Shanxi Province, China (Nos. 201901D111105 and 201901D111114), and Key Research and Development Program of Shanxi Province (No. 202102050201008).

Institutional Review Board Statement: Not applicable.

Informed Consent Statement: Not applicable.

Data Availability Statement: Not applicable.

Conflicts of Interest: The authors declare no conflict of interest.

References

1. Lu, Y.; Gao, X.; Jiang, L.; Chen, Z.; Wang, T.; Jie, J.; Kang, H.; Zhang, Y.; Guo, S.; Ruan, H.; et al. Directly cast bulk eutectic and near-eutectic high entropy alloys with balanced strength and ductility in a wide temperature range. *Acta Mater.* **2017**, *124*, 143–150. [CrossRef]
2. Petch, N. The ductile-brittle transition in the fracture of α-iron: I. *Philos. Mag.* **1958**, *3*, 1089–1097. [CrossRef]
3. Tobler, R.L.; Reed, R. Fatigue crack growth resistance of structural alloys at cryogenic temperatures. In *Advances in Cryogenic Engineering*; Springer: Boston, MA, USA, 1978; pp. 82–90.
4. Gludovatz, B.; Hohenwarter, A.; Catoor, D.; Chang, E.H.; George, E.P.; Ritchie, R.O. A fracture-resistant high-entropy alloy for cryogenic applications. *Science* **2014**, *345*, 1153–1158. [CrossRef] [PubMed]
5. Jo, Y.; Jung, S.; Choi, W.; Sohn, S.S.; Kim, H.; Lee, B.; Kim, N.J.; Lee, S. Cryogenic strength improvement by utilizing room-temperature deformation twinning in a partially recrystallized VCrMnFeCoNi high-entropy alloy. *Nat. Commun.* **2017**, *8*, 15719. [CrossRef]
6. Sun, S.J.; Tian, Y.Z.; Lin, H.R.; Yang, H.J.; Dong, X.G.; Wang, Y.H.; Zhang, Z.F. Achieving high ductility in the 1.7 GPa grade CoCrFeMnNi high-entropy alloy at 77 K. *Mater. Sci. Eng. A* **2019**, *740–741*, 336–341. [CrossRef]
7. Bae, J.W.; Seol, J.B.; Moon, J.; Sohn, S.S.; Jang, M.J.; Um, H.Y.; Lee, B.J.; Kim, H.S. Exceptional phase-transformation strengthening of ferrous medium-entropy alloys at cryogenic temperatures. *Acta Mater.* **2018**, *161*, 388–399. [CrossRef]
8. He, Z.F.; Jia, N.; Ma, D.; Yan, H.L.; Li, Z.M.; Raabe, D. Joint contribution of transformation and twinning to the high strength-ductility combination of a FeMnCoCr high entropy alloy at cryogenic temperatures. *Mater. Sci. Eng. A* **2019**, *759*, 437–447. [CrossRef]
9. Bian, B.B.; Guo, N.; Yang, H.J.; Guo, R.P.; Yang, L.; Wu, Y.C.; Qiao, J.W. A novel cobalt-free FeMnCrNi medium-entropy alloy with exceptional yield strength and ductility at cryogenic temperature. *J. Alloys Compd.* **2020**, *827*, 153981. [CrossRef]
10. Li, Z.; Pradeep, K.G.; Deng, Y.; Raabe, D.; Tasan, C.C. Metastable high-entropy dual-phase alloys overcome the strength-ductility trade-off. *Nature* **2016**, *534*, 227–230. [CrossRef]
11. Zhang, Y.; Zuo, T.T.; Tang, Z.; Gao, M.C.; Dahmen, K.A.; Liaw, P.K.; Lu, Z.P. Microstructures and properties of high-entropy alloys. *Prog. Mater. Sci.* **2014**, *61*, 1–93. [CrossRef]
12. Zhang, Y.; Zhou, Y.J.; Lin, J.P.; Chen, G.L.; Liaw, P.K. Solid-solution phase formation rules for multi-component alloys. *Adv. Eng. Mater.* **2008**, *10*, 534–538. [CrossRef]
13. Yang, X.; Zhang, Y. Prediction of high-entropy stabilized solid-solution in multi-component alloys. *Mater. Chem. Phys.* **2012**, *132*, 233–238. [CrossRef]
14. Senkov, O.N.; Miller, J.D.; Miracle, D.B.; Woodward, C. Accelerated exploration of multi-principal element alloys with solid solution phases. *Nat. Commun.* **2015**, *6*, 6529. [CrossRef]
15. Miracle, D.B. High-entropy alloys: A current evaluation of founding ideas and core effects and exploring "Nonlinear alloys". *JOM* **2017**, *69*, 2130–2136. [CrossRef]

16. Toda-Caraballo, I.; Rivera-Díaz-del-Castillo, P.E.J. A criterion for the formation of high entropy alloys based on lattice distortion. *Intermetallics* **2016**, *71*, 76–87. [CrossRef]
17. Guo, S.; Ng, C.; Lu, J.; Lu, C. Effect of valence electron concentration on stability of fcc or bcc phase in high entropy alloys. *J. Appl. Phys.* **2011**, *109*, 103505. [CrossRef]
18. Zhao, Y.L.; Yang, T.; Zhu, J.H.; Chen, D.; Yang, Y.; Hu, A.; Liu, C.T.; Kai, J.J. Development of high-strength Co-free high-entropy alloys hardened by nanosized precipitates. *Scr. Mater.* **2018**, *148*, 51–55. [CrossRef]
19. Bloomfield, M.E.; Christofidou, K.A.; Jones, N.G. Effect of Co on the phase stability of CrMnFeCoxNi high entropy alloys following long-duration exposures at intermediate temperatures. *Intermetallics* **2019**, *114*, 106582. [CrossRef]
20. George, E.P.; Curtin, W.; Tasan, C.C. High entropy alloys: A focused review of mechanical properties and deformation mechanisms. *Acta Mater.* **2020**, *188*, 435–474. [CrossRef]
21. Wu, X.; Li, Z.; Rao, Z.; Ikeda, Y.; Dutta, B.; Körmann, F.; Neugebauer, J.; Raabe, D. Role of magnetic ordering for the design of quinary TWIP-TRIP high entropy alloys. *Phys. Rev. Mater.* **2020**, *4*, 033601. [CrossRef]
22. Zaddach, A.; Niu, C.; Koch, C.; Irving, D. Mechanical properties and stacking fault energies of NiFeCrCoMn high-entropy alloy. *JOM* **2013**, *65*, 1780–1789. [CrossRef]
23. Okamoto, N.L.; Fujimoto, S.; Kambara, Y.; Kawamura, M.; Chen, Z.M.; Matsunoshita, H.; Tanaka, K.; Inui, H.; George, E.P. Size effect, critical resolved shear stress, stacking fault energy, and solid solution strengthening in the CrMnFeCoNi high-entropy alloy. *Sci. Rep.* **2016**, *6*, 35863. [CrossRef] [PubMed]
24. Olson, G.; Cohen, M. A general mechanism of martensitic nucleation: Part III. Kinetics of martensitic nucleation. *Metall. Trans. A* **1976**, *7*, 1915–1923. [CrossRef]
25. Curtze, S.; Kuokkala, V.T.; Oikari, A.; Talonen, J.; Hänninen, H. Thermodynamic modeling of the stacking fault energy of austenitic steels. *Acta Mater.* **2011**, *59*, 1068–1076. [CrossRef]
26. Ishida, K. Direct estimation of stacking fault energy by thermodynamic analysis. *Phys. Status Solidi A* **1976**, *36*, 717–728. [CrossRef]
27. Grässel, O.; Krüger, L.; Frommeyer, G.; Meyer, L. High strength Fe-Mn-(Al, Si) TRIP/TWIP steels development-properties-application. *Int. J. Plast.* **2000**, *16*, 1391–1409. [CrossRef]
28. Inden, G. The role of magnetism in the calculation of phase diagrams. *Physica B C* **1981**, *103*, 82–100. [CrossRef]
29. Allain, S.; Chateau, J.P.; Bouaziz, O.; Migot, S.; Guelton, N. Correlations between the calculated stacking fault energy and the plasticity mechanisms in Fe-Mn-C alloys. *Mater. Sci. Eng. A* **2004**, *387*, 158–162. [CrossRef]
30. Yakubtsov, I.; Ariapour, A.; Perovic, D. Effect of nitrogen on stacking fault energy of fcc iron-based alloys. *Acta Mater.* **1999**, *47*, 1271–1279. [CrossRef]
31. Zhang, Y.; Zhuang, Y.; Hu, A.; Kai, J.J.; Liu, C.T. The origin of negative stacking fault energies and nano-twin formation in face-centered cubic high entropy alloys. *Scr. Mater.* **2017**, *130*, 96–99. [CrossRef]
32. Han, Z.; Liang, S.; Yang, J.; Wei, R.; Zhang, C. A superior combination of strength-ductility in CoCrFeNiMn high-entropy alloy induced by asymmetric rolling and subsequent annealing treatment. *Mater. Charact.* **2018**, *145*, 619–626. [CrossRef]
33. Tong, Y.; Chen, D.; Han, B.; Wang, J.; Feng, R.; Yang, T.; Zhao, C.; Zhao, Y.; Guo, W.; Shimizu, Y.; et al. Outstanding tensile properties of a precipitation-strengthened FeCoNiCrTi0. 2 high-entropy alloy at room and cryogenic temperatures. *Acta Mater.* **2019**, *165*, 228–240. [CrossRef]
34. Mahajan, S.; Chin, G.Y. Formation of deformation twins in f.c.c. crystals. *Acta Metall.* **1973**, *21*, 1353–1363. [CrossRef]
35. Mahajan, S.; Green, M.L.; Brasen, D. A model for the FCC→HCP transformation, its applications, and experimental evidence. *Metall. Trans. A* **1977**, *8*, 283–293. [CrossRef]
36. Wong, S.L.; Madivala, M.; Prahl, U.; Roters, F.; Raabe, D. A crystal plasticity model for twinning- and transformation-induced plasticity. *Acta Mater.* **2016**, *118*, 140–151. [CrossRef]